

# Optical Satellite Sensor and Positioning Accuracy Assessment for The Hongqi-H9 Wide-Range Satellite in Different Terrains

**Wenping Song**

Tongji University <https://orcid.org/0000-0002-1171-4266>

**Jianxiong Wang** (✉ [jianxiongw@126.com](mailto:jianxiongw@126.com))

Water Conservancy Academy, YunNan Agricultural University

**Yang Bai**

Changuang Satellite Technology Co.,LTD

**Linhui Wang**

Hunan University of Science and Engineering

**Xiang Li**

Changuang Satellite Technology Co.,LTD

**Shiqiang Tian**

Changuang Satellite Technology Co.,LTD

**Xianyang Qi**

Changuang Satellite Technology Co., LTD

---

## Research

**Keywords:** Geometric positioning, Different terrains, the Hongqi-H9 satellite, Accuracy assessment

**Posted Date:** October 6th, 2020

**DOI:** <https://doi.org/10.21203/rs.3.rs-57295/v1>

**License:** © ⓘ This work is licensed under a Creative Commons Attribution 4.0 International License.

[Read Full License](#)

---

**Version of Record:** A version of this preprint was published on January 6th, 2021. See the published version at <https://doi.org/10.1186/s13638-020-01876-1>.

# Optical Satellite Sensor and Positioning Accuracy Assessment for the Hongqi-H9 Wide-Range Satellite in Different Terrains

Wenping Song<sup>1</sup>, Jianxiong Wang<sup>2\*</sup>, Yang Bai<sup>3</sup>, Linhui Wang<sup>4</sup>, Xiang Li<sup>3</sup>, Shiqiang Tian<sup>3</sup> and Xianyang Qi<sup>3</sup>

\*Correspondence:

jianxiongw@126.com

<sup>2</sup>Water Conservancy Academy, YunNan Agricultural University, 452 Fengyuan Road, 650201 Kunming, China  
Full list of author information is available at the end of the article

## Abstract

The Hongqi-H9 wide-range satellite, which was launched on January 15, 2020, has a resolution of less than 1 m and a swath width of 136 km. This satellite is the largest sub-meter level satellite worldwide and the first ton-level commercial remote sensing satellite in China. In particular, this satellite can acquire sub-meter image data for an area of approximately 1,000 km<sup>2</sup> per second and full-coverage image information for an area of more than 1,000,000 km<sup>2</sup>. This study was aimed at assessing the geometric positioning accuracy of the Hongqi-H9 satellite considering three aspects, namely, the circle error accuracy, rational polynomial coefficient based direct geometric positioning accuracy and ground control point based absolute positioning accuracy under urban, plain, and mountainous areas, with different topographies. The results of the conducted experimental investigation indicated that the Hongqi-H9 satellite could exhibit a high positioning accuracy in planar and vertical directions for different terrains. In particular, for areas with a low topography and few surface structures, the geometric positioning accuracy of the Hongqi-H9 satellite imagery was less than 4 and 2 m in the planimetry and elevation directions, respectively. These characteristics can promote the application of the Hongqi-H9 satellite images in agricultural surveys, target detection, and land surveys, among other domains.

**Keywords:** Geometric positioning; Different terrains; the Hongqi-H9 satellite; Accuracy assessment

## 1. Introduction

Despite the rapid advancement in satellite remote sensing technology, two key requirements to obtain high spatial resolution satellite images remain to be attained [1-3]. The first requirement corresponds to the fixed-point fast revisit capability, which is primarily influenced by the timeliness of the satellites [4-5]; for instance, satellites can generally provide real-time images of disaster areas within a few minutes in natural disaster events [6]. The second requirement corresponds to the prompt updating capacity for a large-scale area, which mainly depends on the swath width of the satellite. This aspect can facilitate the rapid monitoring of construction areas [7], daily distribution survey of marine vessels [8], and agricultural surveys, among other applications, in which large-scale time series satellite images must be acquired in a small period.

Changguang is in the process of deploying the “Jilin-1” optical remote sensing satellite constellation in two phases [9-10]: The first phase involves placing 60 satel-

lites in orbit, thereby allowing the revisitation of key regions worldwide within 30 min and the observation of more than 800 target areas worldwide every day. In the second phase, 138 satellites will be present in orbit, thereby enabling the revisitation of any area worldwide within 10 min. The first batch of satellites of the “Jilin-1” optical remote sensing constellation, including the optical A satellite, smart video 01/02 satellite, and smart verification satellite, was launched successfully on October 15, 2015, and these satellites have been in orbit for 4.5 y. Subsequently, the video 03-08 satellites were launched sequentially. The Jilin-1KF01A satellite (Hongqi-H9 wide-range satellite, hereafter referred to as the Hongqi-H9 satellite), which was successfully launched on January 15, 2020, is the largest sub-meter level satellite worldwide and the first ton-level commercial remote sensing satellite in China, with a resolution of less than 1 m and a swath width of 136 km. The Hongqi-H9 satellite can acquire sub-meter image data at a rate of approximately 1,000 km<sup>2</sup> per second and the full-coverage image information for an area of more than 1000,000 km<sup>2</sup>. The sensor information for the Jilin-1KF01A satellite is presented in Table 1 [11].

Table 1: Characteristics of the Hongqi-H9 satellite.

Specification	Panchromatic	Multispectral
Field of view	16.1	16.1
Focal length	4850 mm	4850 mm
Ground sample distance	0.75 m	3.0 m
Swath width	136 km	136 km
Attitude stability	<0.0005/s	<0.0005/s
Signal-Noise ratio	>100:1	>100:1

In general, the resolution and swath width of satellite images are inversely related, that is, the swath width decreases as the resolution increases [12]. Conventionally, the satellite swath width is increased by stitching multiple lenses whose optical axis does not point to the center of the Earth [9]. However, this type of optical imaging system is only suitable when the field of view is not excessively large (approximately 10). According to Table 1, the field of view of the Hongqi-H9 satellite is 16.1. Consequently, applying multi-lens stitching may significantly increase the difference in the pixel resolution between the edge and center of the image plane [13]. Moreover, the shift differences in the images caused by the curvature and rotation of the Earth, among other factors, may lead to different sampling effects at different viewing positions, leading to a deteriorated image quality [14]. The Hongqi-H9 satellite avoids the projection distortion caused by multiple lenses by using a single lens whose optical axis points to the center of the Earth. In this case, the resolutions of the center and edge of the field of view are nearly equivalent, thereby facilitating the image processing [11]. Nevertheless, a single lens cannot be used to achieve a focal length of 4,850 mm and field of view of 16.1. In particular, the Hongqi-H9 satellite adopts the Cook three-mirror anastigmat (TMA) system, as shown in Fig. 1 [15-16]. The Cook TMA system can eliminate the central block from the aperture by increasing the off-axis field of view [17]. Therefore, the clear aperture of the field of view and the mirror is completely off-axis, forming a coaxial system in which the field of view and aperture are off-axis. In this configuration, the position change between any two mirrors approximately 1 m apart is not more than 5 m, the shape of the large aspheric mirror corresponds to a wavelength of more than 1/50, and the original dynamic modulation transfer function is larger than 0.16 [11]. Consequently,

the imaging clarity and geometric accuracy can be enhanced even when vibration and temperature changes occur.

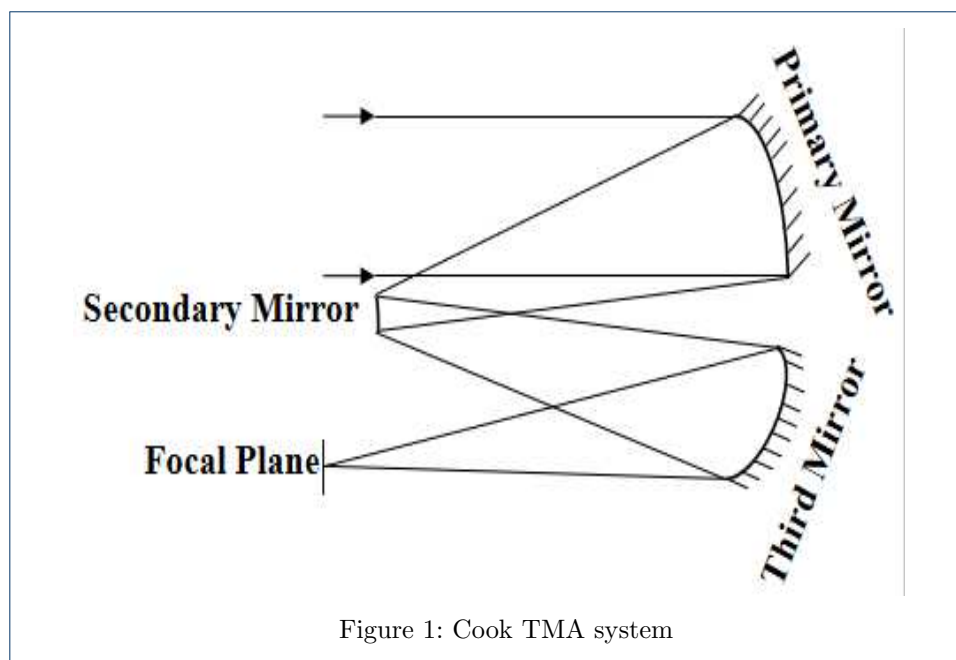


Figure 1: Cook TMA system

Considering the characteristics of the Hongqi-H9 satellite, the objective of this study was to evaluate a novel optical satellite sensor and assess the geometric positioning accuracy of the Hongqi-H9 satellite in areas with three different topographies, specifically, urban, plain, and mountainous areas. In experiments, the imagery obtained through the Hongqi-H9 satellite was evaluated in terms of the circle error (CE) accuracy, vendor-provided rational polynomial coefficient (RPC) based direct geometric positioning accuracy and ground control point (GCP) based absolute positioning accuracy. From the experimental study, several conclusions were obtained regarding the newly launched Hongqi-H9 satellite. It was noted that the basic product could realize regional mapping and meet the application requirements.

The remaining paper is organized as follows. After the introduction of the Hongqi-H9 satellite, Section 2 introduces the geometric positioning assessment methods and criteria. Section 3 describes the study area and data used. The experimental results and discussion are presented in Section 4, and the concluding remarks are presented in Section 5.

## 2. Methods

Generally, satellite images can be used to evaluate the geometric positioning accuracy by using two approaches [18]. In the first approach, high-performance sensor structures and parameters can be used to realize the geometric transformation from the image space to the ground space [19-22]. The second approach is based on the use of a rational function model (RFM), which exploits the constraints between different images [23-25]. Nevertheless, the error contained in the RPCs may destroy the photogrammetric relation and deteriorate the geometric performance of

the obtained high-resolution images. In particular, the accuracy of the first evaluation approach is more accurate. In this work, a data-driven evaluation method was employed, as described in the following subsections.

## 2.1 Preprocessing

In general, the vendor-provided RPCs can replace the position and attitude parameters of satellite sensors [26]. Different RPCs for different data processing phases, containing different degrees of errors, can be defined according to the exterior orientation parameters by using the rigorous sensor model (RSM) [27-28]. In this study, the existing RPCs were extracted through radiation and geometric correction. These RPCs were solved using a terrain-independent method. Specifically, first, image grids were established in the image space, and later, a three-dimensional (3D) coordinate grid area was established in the ground space. In this process, the RSM calculated the point coordinates of the ground grids, and the ground 3D grids were divided into more than three layers in the elevation direction. Finally, the RPCs were calculated using the least squares method according to the established image and ground grids [29]. For convenience, all the satellite imagery data, GPS points, and accuracy results were defined according to the WGS84 coordinate system.

## 2.2 RPCs-based block adjustment model

The RFM is a traditional expression of the satellite sensor model, in which rational polynomials are used to ensure the correspondence between the image and ground points, as indicated in equation 1.

$$\begin{cases} x_n = \frac{Num_1(B_n, L_n, H_n)}{Den_1(B_n, L_n, H_n)} \\ x_n = \frac{Num_1(B_n, L_n, H_n)}{Den_1(B_n, L_n, H_n)} \end{cases} \quad (1)$$

where  $(x_n, y_n)$  represent normalized image coordinates, corresponding to the normalized coordinates  $(B_n, L_n, Z_n)$  in the ground space.  $Num_i(B_n, L_n, Z_n)$  ( $i = 1, 2$ ) and  $Den_i(B_n, L_n, Z_n)$  ( $i = 1, 2$ ) denote the rational polynomials. As described in the literature [30], linear polynomials are used to correct the distortions caused by optical projection; quadratic polynomials are used to correct the errors induced by the Earth curvature, lens distortion, and atmospheric refraction; and the other unknown distortions are compensated using the cubic polynomial.

Compared with that in ground space, the compensation in image space is more rigorous theoretically [31], as indicated in equation (2).

$$\begin{cases} x' = a_0 + a_1x + a_2y \\ y' = b_0 + b_1x + b_2y \end{cases} \quad (2)$$

where  $(x', y')$  denote the image points measured corresponding to the ground points;  $(x, y)$  denote the image coordinate values of the ground points calculated using equation (2);  $(a_0)$  and  $(b_0)$  denote the shift orientation parameters; and  $a_i$  ( $i = 0, 1, 2$ ) and  $b_i$  ( $i = 0, 1, 2$ ) denote the affine transformation orientation parameters,

where  $a_i (i = 0, 1, 2)$  and  $b_i (i = 0, 1, 2)$  are used to correct errors in the column and row directions, respectively.

Therefore, the RPCs-based block adjustment model can be constructed in matrix form as shown in equation (3), according to equations (1) and (2) [32-33]:

$$V = At + BX - L \quad (3)$$

where,

$$V = [V_x, V_y]^T$$

$$A = \begin{bmatrix} \frac{\partial x}{\partial a_0} & \cdots & \frac{\partial x}{\partial a_1} & \frac{\partial x}{\partial a_2} \\ \frac{\partial y}{\partial b_0} & \cdots & \frac{\partial y}{\partial b_1} & \frac{\partial y}{\partial b_2} \\ \frac{\partial x}{\partial n} & \frac{\partial x}{\partial L_n} & \frac{\partial x}{\partial n} \\ \frac{\partial y}{\partial B_n} & \frac{\partial y}{\partial L_n} & \frac{\partial y}{\partial Z_n} \end{bmatrix}$$

$$B = \begin{bmatrix} \frac{\partial x}{\partial n} & \frac{\partial x}{\partial L_n} & \frac{\partial x}{\partial n} \\ \frac{\partial y}{\partial B_n} & \frac{\partial y}{\partial L_n} & \frac{\partial y}{\partial Z_n} \end{bmatrix}$$

$$t = [\Delta a_0 \quad \Delta a_1 \quad \Delta a_2 \quad \Delta b_0 \quad \Delta b_1 \quad \Delta b_2]^T$$

$$X = [\Delta B_n \quad \Delta L_n \quad \Delta H_n]^T$$

### 2.3 Accuracy evaluation

In this work, the geometric positioning accuracy of the Hongqi-H9 satellite imagery under three different terrains was evaluated considering control-based and non-control-based geometric positioning accuracies. Among these, the non-control-based geometric positioning accuracy included two parts: accuracy evaluation based on circular probability errors and on direct forward intersection by using vendor-provided RPCs [34-35].

To examine the control-based geometric positioning accuracy and that based on direct forward intersection by using the vendor-provided RPCs, high-precision GPS measured points ( $B_{GPS}, L_{GPS}, H_{GPS}$ ) and their corresponding solved coordinate values ( $B_i, L_i, H_i$ ) ( $i = 1, 2, \dots, n$ ) were determined to obtain the root mean squared errors (RMSEs), as shown in equation (4).

$$\left\{ \begin{array}{l} RMSE_B = \sqrt{\frac{\sum_{i=1}^n (B_{GPS} - B_i)^2}{n}} \\ RMSE_L = \sqrt{\frac{\sum_{i=1}^n (L_{GPS} - L_i)^2}{n}} \\ RMSE_H = \sqrt{\frac{\sum_{i=1}^n (H_{GPS} - H_i)^2}{n}} \end{array} \right. \quad (4)$$

The accuracy evaluation based on circular probability errors [36] was performed in three phases. (1) Obtaining two geometric positioning error sets X and Y in the longitude and latitude directions, respectively, which correspond to the differences between the point coordinates measured on the image and the corresponding GPS measured points. (2) Determining the means  $\mu_x$  and  $\mu_y$ , RMSEs  $\sigma_x$  and  $\sigma_y$ , and correlation coefficient  $\rho$  for sets X and Y. (3) Ensuring that the geometric positioning errors with systematic errors and strong correlations in all the directions follow a normal distribution. The joint density function in the polar coordinate system was defined as in Formula (5) [37]:

$$\frac{1}{2\pi\sigma_x\sigma_y\sqrt{1-\rho^2}} \int_0^{CE90} \int_0^{2\pi} r * \exp\left\{-\frac{1}{2(1-\rho)} \left[ \frac{(r\cos\theta - \mu_x)^2}{\sigma_x^2} - \frac{2\rho(r\cos\theta - \mu_x)(r\sin\theta - \mu_y)}{\sigma_x\sigma_y} + \frac{(r\sin\theta - \mu_y)^2}{\sigma_y^2} \right]\right\} drd\theta = P \quad (5)$$

where,  $X = r\cos\theta, Y = r\sin\theta, r = \sqrt{(X^2 + Y^2)}$ . The CE90 was solved to measure the non-control-based geometric positioning accuracy.

### 3. Study area and data

The considered study areas are located in three regions with different terrains in China (Fig. 2). The urban area has many high-rise buildings, and the plain and mountainous areas have rough terrains. These feature ranges are considerably different in terms of the terrains and surface coverage. The urban, plain, and mountainous study areas cover approximately 550 km<sup>2</sup>, 600 km<sup>2</sup>, and 720 km<sup>2</sup>, respectively. The urban and plain areas traverse the altitudinal range of 0–150 m. The mountainous area exhibit a high variability of slopes with varying orientations of the ridges and deep valleys; moreover, this area includes few notable water bodies.

The satellite images of the three study areas were acquired during the winter when the surface vegetation coverage was relatively simple. Moreover, the overlaps of the stereo images for the three areas were more than 80%, and the ground sampling distance was approximately 0.75 m. Fig. 2 illustrates the coverage of the three study areas with different terrains in China. The urban area ranged from 121.267E to 121.592E and from 30.018N to 31.316N in the longitudinal and latitudinal directions, respectively, and the imagery data were collected in February 2020. The plain area ranged from 120.90E to 121.338E and from 30.90N to 31.20N in the longitudinal and latitudinal directions, respectively, and the satellite imagery data were collected in 2020, with a field of view of 16.1. The mountainous area ranged from 100.60E to 101.228E and from 25.042N to 25.3N in the longitudinal and latitudinal directions, respectively, and the satellite imagery data were acquired on March 19, 2020.

To perform absolute accuracy assessments, accurate and independent reference data are required [38-39]. The reference data should be at least three times more accurate than the evaluated data [40]. Therefore, in this work, we considered high-quality GPS points with an accuracy of more than 5 cm, which satisfy the accuracy requirement, and thus, do not adversely affect the evaluation. For the urban, plain,

and mountainous areas, the number of GPS points for the comparative experiments and accuracy assessment was 32, 18, and 25, respectively.

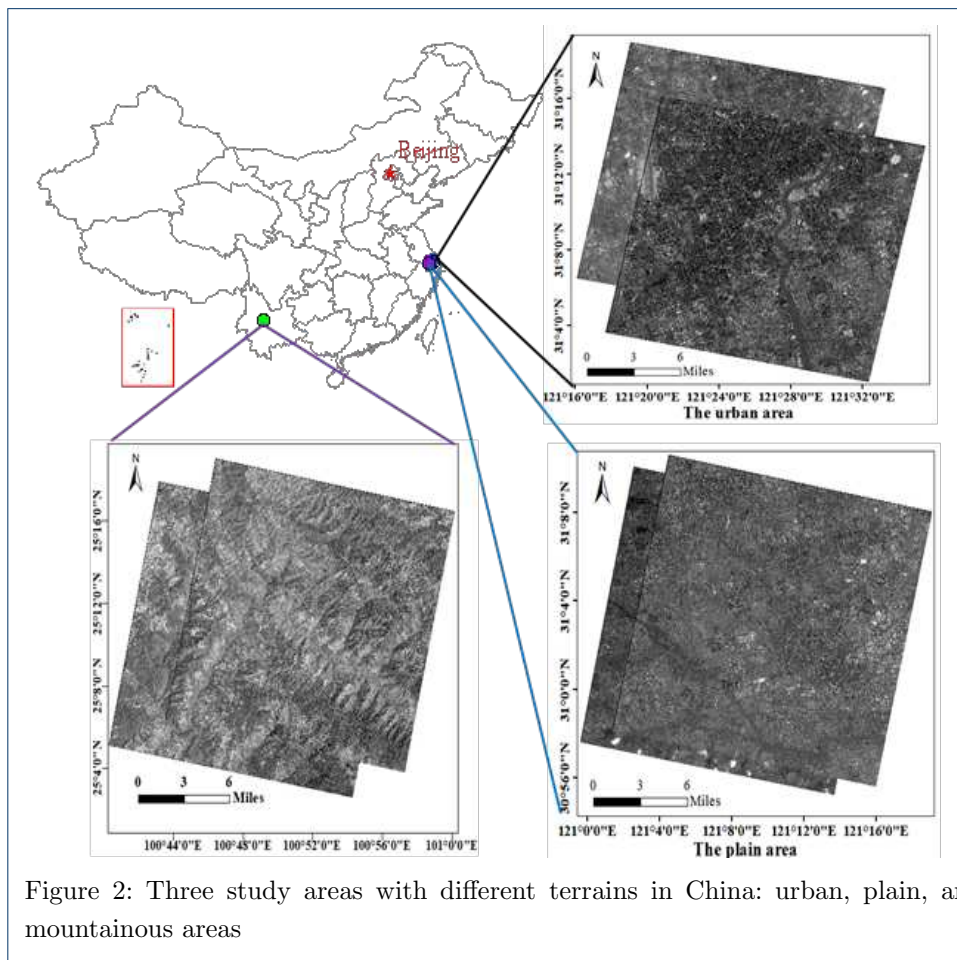


Figure 2: Three study areas with different terrains in China: urban, plain, and mountainous areas

### 4.Results and Discussion

#### 4.1 Evaluation of geometric positioning accuracy without ground control points

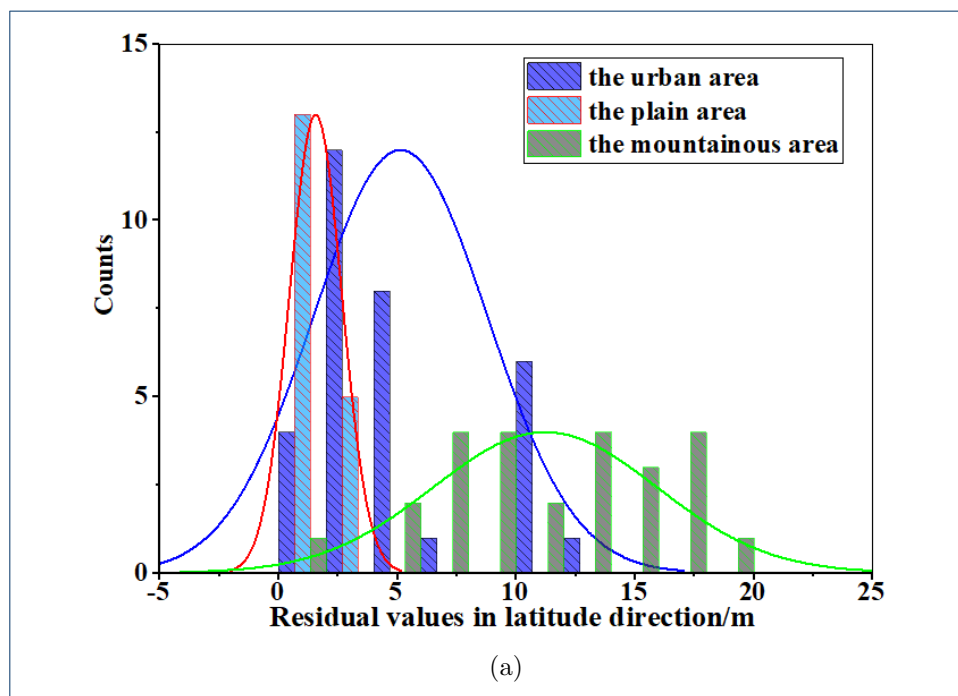
The geometric positioning accuracy assessment of the Hongqi-H9 satellite imagery without using ground control points involved two parts: accuracy evaluation based on circular probability errors and that of the direct forward intersection by using vendor-provided RPCs.

##### *Accuracy evaluation based on circular probability errors*

The accuracy based on the circular probability errors was calculated according to the three phases described in Section 2.3. The residuals, including the errors in the latitude and longitude directions, for the Hongqi-H9 satellite imagery under three different terrains are illustrated in Fig. 3. In Fig. 3, the x and y axes denote the residual values for the three study areas and the corresponding residual counts, respectively. In addition, the residual fitting results for the Hongqi-H9 satellite imagery under three different terrains, obtained using normal distribution functions, are presented. It can be noted that the circular probability error based accuracy

for the plain area has smaller confidence intervals in all the directions compared to those for the urban and mountainous areas. In particular, in the latitudinal direction, except for certain outliers caused by human factors, the geometric positioning accuracies of the Hongqi-H9 satellite imagery in the plain and urban areas are approximately 3–5 m and less than 7 m, respectively, which are considerably superior than the accuracy for the mountainous area (approximately 10–16 m), nearly consistent with the positioning accuracy in the longitudinal direction. Moreover, in the longitudinal direction, the Hongqi-H9 satellite images in the plain and urban areas exhibit nearly equivalent positioning performances (less than 5 m). The planar geometric positioning accuracy for the plain area is slightly superior than that for the urban area, although it is considerably higher than that for the mountainous area, as shown in Fig. 4. A possible explanation for this difference is that the stereo images in the mountain area have a weak intersection angle, which decreases the geometric positioning performance to a certain extent. In other words, the positioning performance in the mountainous area can be improved by improving the intersection condition.

Table 2 summarizes the results of the geometric positioning based on the circular probability errors. It can be noted that the images pertaining to the plain area (CE90 4.5051 m) correspond to a slightly higher positioning performance than that for the urban area (CE90 6.7216 m) and exhibit a smaller span of residuals, indicating the higher stability of positioning in the plain area. However, for the mountainous area, the maximum circular probability error in the planimetry direction is 15.5212 m. Therefore, the Hongqi-H9 satellite imagery can exhibit a circle probability error based accuracy of less than 5 m, less than 7 m, and 15.5212 m in the plain, urban, and mountainous areas, respectively.



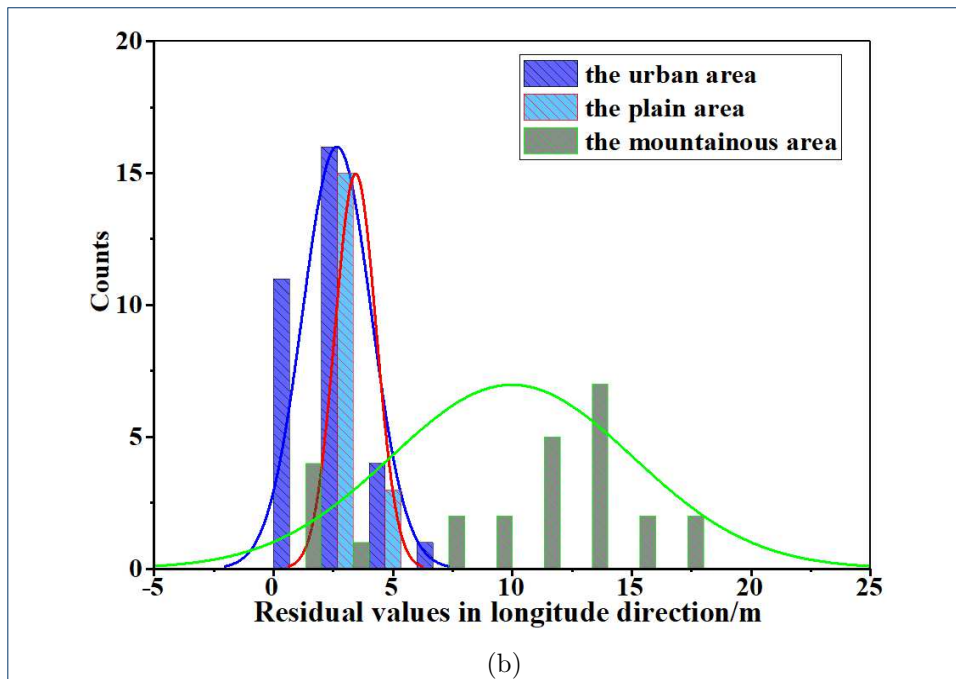


Figure 3: Residuals of the Hongqi-H9 imagery under three different terrains in the (a) latitude and (b) longitude directions. The x and y axes correspond to the residual values of the three different study areas and the corresponding residual counts, respectively. The residual fitting results for the Hongqi-H9 satellite imagery under three different terrains, obtained using the normal distribution functions are also presented.

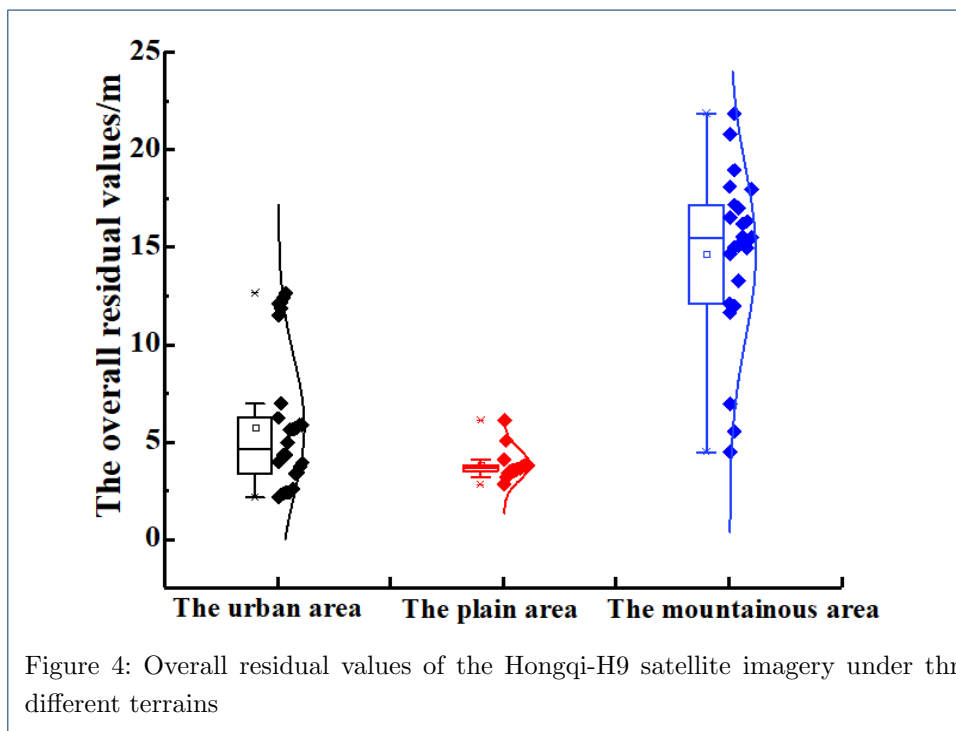


Figure 4: Overall residual values of the Hongqi-H9 satellite imagery under three different terrains

Table 2: Accuracy evaluation based on circular probability errors for the three terrains.

Area	Urban	Plain	Mountainous
CE90/m	6.7216	4.5051	15.5212

*Accuracy evaluation of direct forward intersection by using vendor-provided RPCs*

After the radiometric correction, the vendor-provided RPCs were extracted from the structures and parameters of the RSM, which can be used to construct the RFM for the geometric positioning by replacing the RSM. In the experimental evaluation of the direct forward intersection using the vendor-provided RPCs, the accuracy of all the GPS points was less than 5 cm, and the weights were considered to be equivalent. For the corresponding feature points, high-criteria manual selection was adopted to ensure the sub-pixel level characteristics, which can satisfy the requirements of the geometric positioning.

Fig. 5 shows the results for the direct positioning accuracy obtained using the vendor-provided RPCs in the WGS84 coordinate system. The x-axis is separated into the planar and vertical accuracies, for each of which, the geometric positioning residuals and Gauss fitting curves of the three study areas are shown in the figure. The y-axis shows the corresponding residual values. It can be noted that the error values in both the planimetry and elevation directions are similar, even though the positioning accuracy in the mountainous area is worse than that in the plain and urban areas. Specifically, as indicated in Table 2, for the urban area, the mean errors in the planimetry and elevation directions are 17.3303 m and 11.3748 m, and the RMSEs are 17.8739 m and 11.6761 m, respectively. Similar to these values, the plain area exhibits, in the planimetry and vertical directions, mean errors of 15.9954 m and 12.2240 m, and RMSEs of 16.3902 m and 12.3994 m, respectively. In the mountainous area, the planar and vertical RMSEs are 21.2616 m and 17.4499 m, respectively. Overall, for all three terrains, the geometric positioning accuracy determined using the vendor-provided RPCs is less than 20 m and 15 m in the planimetry and vertical directions, respectively.

Moreover, the accuracy of the direct forward intersection obtained using the vendor-provided RPCs was worse than that based on the circular probability errors, as indicated by the comparison of the values presented in Tables 1 and 2. A possible explanation for this difference is that the vendor-provided RPCs still contain systematic errors, which considerably deteriorate the geometric positioning. Furthermore, the angles for the cross track stereo images are influence the direct positioning accuracy. In this regard, the geometric positioning accuracy can be improved by reducing the system errors in the vendor-provided RPCs.

Table 3: Mean errors and RMSEs of the direct forward intersection, obtained using the vendor-provided RPCs, for three different terrains.

Category	Urban area		Plain area		Mountainous area	
Direction	Planar/m	Vertical/m	Planar/m	Vertical/m	Planar/m	Vertical/m
Mean error	17.3303	11.3748	15.9954	12.2240	21.0881	17.0761
RMSEs	17.8739	11.6761	16.3902	12.3994	21.2616	17.4499

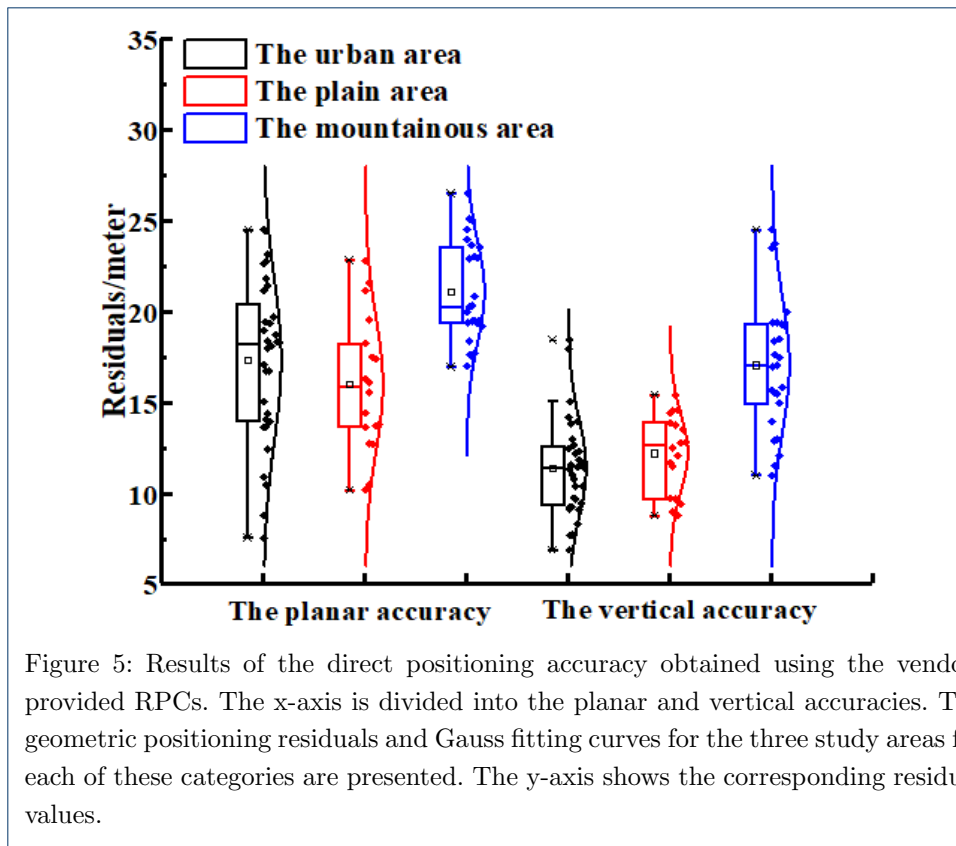


Figure 5: Results of the direct positioning accuracy obtained using the vendor-provided RPCs. The x-axis is divided into the planar and vertical accuracies. The geometric positioning residuals and Gauss fitting curves for the three study areas for each of these categories are presented. The y-axis shows the corresponding residual values.

#### 4.2 Evaluation of the absolute positioning accuracy

The absolute geometric positioning accuracy can be evaluated considering external orientation elements or GCPs, using the external reference values as a comparison benchmark to reflect the deviation indicated by the RMSEs. As a significant evaluation criterion, it can indicate the accuracy and performance of the satellite imagery for any geometric location. As mentioned previously, 32, 18 and 25 GPS points were measured for the urban, plain and mountainous areas, respectively. In this experiment, five GPS points having nearly equivalent distributions were selected as the control points, and the remaining GPS points were used to evaluate the accuracy. Moreover, the affine transformation model was used for the bias compensation in the image space.

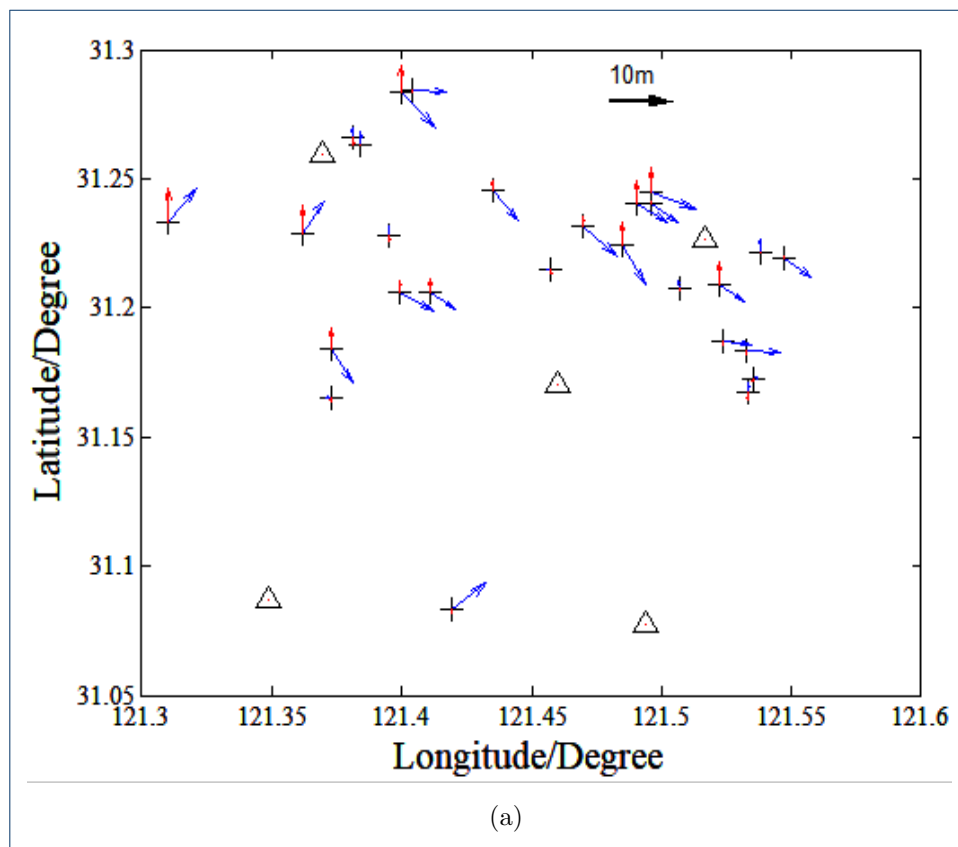
Fig. 6 shows the geometric positioning error bar graphs using the five GCPs. The black crosses represent the point positions in the WGS84 coordinate system, and the blue and red arrows indicate the plane and elevation errors, respectively. As shown in Fig. 5, the Hongqi-H9 satellite imagery under three different terrains exhibit different geometric positioning performances, all of which are sufficient to realize high-resolution mapping.

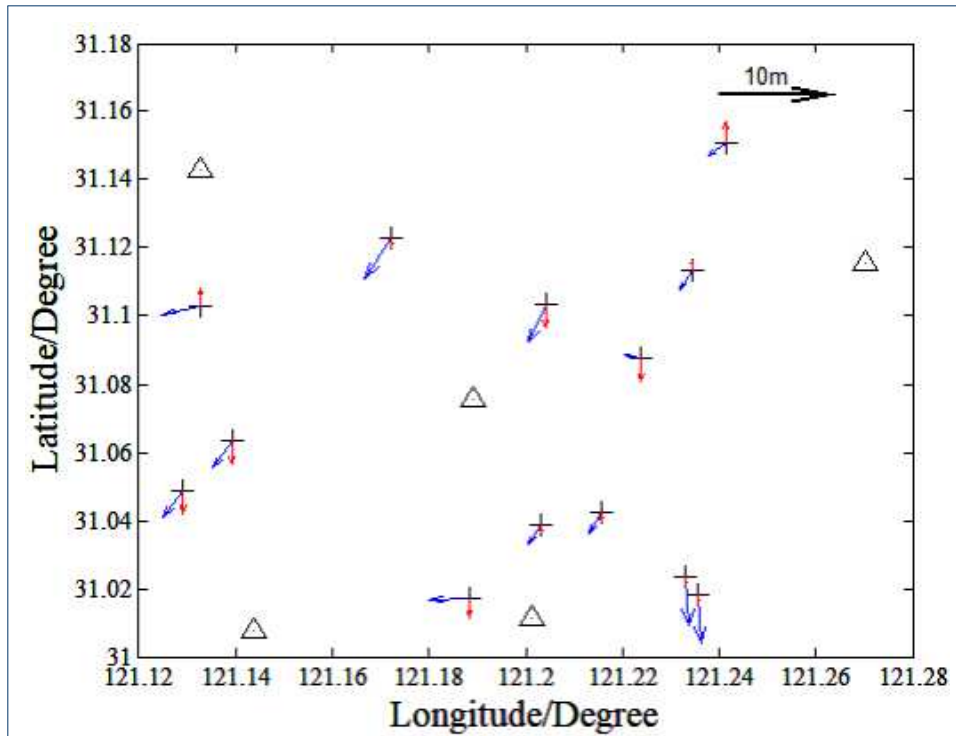
The results of the absolute positioning accuracy are summarized in Table 3. The geometric positioning accuracy is presented in terms of the latitudinal, longitudinal, and vertical direction. From Table 3, it can be noted that the Hongqi-H9 satellite exhibits the highest geometric positioning performance in the plain area, with a positioning accuracy of 3.2448 m, 1.6639 m, and 1.7466 m in the latitudinal, longi-

tudinal, and elevation directions, respectively, when using the five GPS points. For the urban area, the positioning accuracy is slightly poor: 3.4815 m, 4.4756 m, and 2.7262 m in the latitudinal, longitudinal, and elevation directions, respectively. The worst geometric positioning corresponds to the mountainous area, with accuracies of 4.2622 m, 4.9386 m, and 4.9217 m in the latitudinal, longitudinal, and elevation directions, respectively. Overall, based on the experimental data, it can be considered that the Hongqi-H9 satellite imagery can achieve a high positioning accuracy in the planar and vertical directions under different terrains. Specifically, for areas with a low topography and few surface structures, the geometric positioning accuracy of the Hongqi-H9 satellite imagery can be less than 4 m and 2 m in the planimetry and elevation directions, and thus, the Hongqi-H9 satellite images can be applied to realize agricultural surveys and target detection, among other applications.

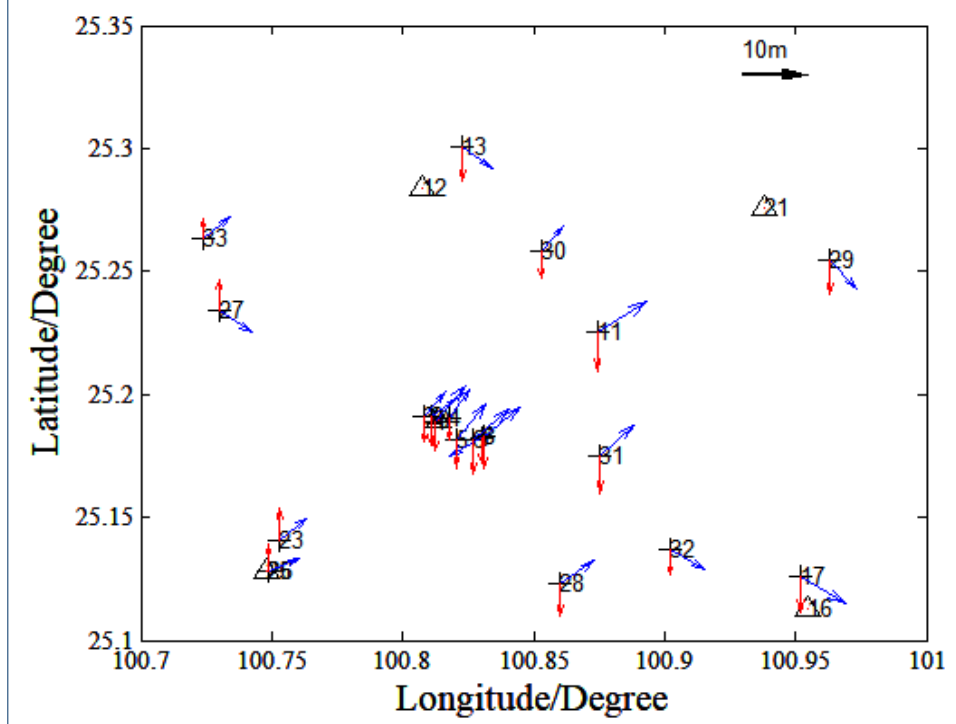
Table 4: Results of the absolute positioning accuracy for the Hongqi-H9 satellite under different terrains.

RMSEs	Directions		
	Latitude	Longitude	Elevation
Urban area/ m	3.4815	4.4756	2.7262
Plain area/m	3.2448	1.6639	1.7466
Mountainous area/m	4.2622	4.9386	4.9217





(b)



(c)

Figure 6: Geometric positioning error bar graphs when using five GCPs. The black crosses represent the point positions in the WGS84 coordinate system, and the blue and red arrows indicate the plane and elevation errors, respectively. (a), (b) and (c) show the results for the urban, plain, and mountainous areas, respectively.

## 5. Conclusions

Considering the characteristics of the Hongqi-H9 satellite, which is the largest sub-meter level satellite worldwide and the first ton-level commercial remote sensing satellite in China [11], this study was aimed at examining the geometric positioning accuracy for the Hongqi-H9 wide-range satellite images under regions with three different topographies, specifically, urban, plain, and mountainous areas. To ensure the feasibility and effectiveness of the assessment, experiments pertaining to the Hongqi-H9 satellite were conducted considering the study area and imagery data, and the evaluation was performed considering three aspects, namely, the CE accuracy, RPC-based direct geometric positioning accuracy, and GCP-based absolute positioning accuracy. The experimental results clarified the geometric positioning performance of the Hongqi-H9 satellite imagery under three different areas with different terrains. From these findings, the following key conclusions were derived for the imagery data of the newly launched Hongqi-H9 satellite:

(1) The Hongqi-H9 satellite imagery could achieve a circle probability error based accuracy of less than 16 m without using any GCPs. In the comparison experiments, the planar geometric positioning performance for the plain and urban areas was nearly equivalent and better than that for the mountainous area.

(2) Under all three terrains, the geometric positioning performance determined using the vendor-provided RPCs was less than 20 m and approximately 15 m in the planimetry and vertical directions, respectively. Moreover, the error values in the planimetry and elevation directions were similar, even though the positioning accuracy in the mountainous area was still worse than that in the plain and urban areas.

(3) The accuracy of the direct forward intersection obtained using the vendor-provided RPCs was relatively worse compared to the circular probability error based accuracy due to the large systematic errors contained in the vendor-provided RPCs, which led to a considerably deterioration in the geometric positioning.

(4) In terms of the absolute geometric positioning, the Hongqi-H9 satellite imagery could achieve a high positioning accuracy in the planar and vertical directions under different terrains. In particular, for areas with a low topography and few surface structures, the geometric positioning accuracy of the Hongqi-H9 satellite imagery was less than 4 and 2 m in the planimetry and elevation directions, respectively, and thus, the Hongqi-H9 satellite images can be applied for agricultural surveys, target detection, and in other fields.

Overall, as the largest sub-meter level satellite worldwide and the first ton-level commercial remote sensing satellite in China [11], the Hongqi-H9 satellite exhibits not only an excellent fixed-point revisitation capability and prompt updating capacities for a large-scale area, but also a high positioning performance through the across-track stereo imagery, and thus, it can be widely used in land surveying and mapping, agricultural estimation and analysis, and such applications.

### Abbreviations

TMA: Three Mirror Anastigmat; RPC: Rational Polynomial Coefficient; CE: Circle Error; GCP: Ground Control Point; RFM: Rational Function Model; RSM: Rigorous Sensor Model; 3D: Three Dimensional; GPS: Global Positioning System; WGS84: World Geodetic System-1984; RMSEs: Root Mean Squared Errors;

### Competing interests

The authors declare that they have no competing interests.

### Author's contributions

WPS performed the experiments and wrote the manuscript. JXW advised on the manuscript and provided funding support. YB revised the manuscript. XL, SQT and XYQ provided the experimental data.

### Acknowledgements

The authors would like to thank Mr. Changling Niu from Qingdao Geotechnical Investigation Surveying Research Institute for his suggestions on this research work. The authors also would like to appreciate the data support from Changguang Satellite Technology Co., LTD, Changchun, China.

### Availability of data and materials

Data sharing not applicable to this article as no datasets were generated or analyzed during the current study.

### Author details

<sup>1</sup>College of Surveying and Geo-informatics, Tongji University, 1239 Siping Road, 200092 Shanghai, China. <sup>2</sup>Water Conservancy Academy, YunNan Agricultural University, 452 Fengyuan Road, 650201 Kunming, China. <sup>3</sup>Changguang Satellite Technology Co., LTD, 1299 Mingxi Road, 130102 Changchun, China. <sup>4</sup> School of Electronics and Information Engineering, Hunan University of Science and Engineering, 130 Yangzitang Road, 425199 Yongzhou, China.

### References

- [1] J. C. White, N. C. Coops, M. A. Wulder, M. Vastaranta, T. Hilker, P. Tompalski, Remote sensing technologies for enhancing forest inventories: A review. *Canadian Journal of Remote Sensing*. 42(5), 619-641 (2016).
- [2] T. E. Shaw, S. Gascoin, P. A. Mendoza, F. Pellicciotti, J. McPhee, Snow Depth Patterns in a High Mountain Andean Catchment from Satellite Optical Tristereoscopic Remote Sensing. *Water Resources Research*. 56(2), 1-23 (2020).
- [3] J. Wang, D. Yang, M. Detto, B. W. Nelson, M. Chen, K. Guan, J. Wu, Multi-scale integration of satellite remote sensing improves characterization of dry-season green-up in an Amazon tropical evergreen forest. *Remote Sensing of Environment*. 246, 865-881 (2020).
- [4] W. G. Han, J. Matthew, Near real-time satellite data quality monitoring and control. 2016 IEEE International Geoscience and Remote Sensing Symposium (IGARSS). 206-209 (2016).
- [5] T. M. Pham, R. Farrell, L. Tran, Revisiting the MIMO capacity with per-antenna power constraint: Fixed-point iteration and alternating optimization. *IEEE Transactions on Wireless Communications*. 18(1), 388-401 (2018).
- [6] N. Said, K. Ahmad, M. Riegler, K. Pogorelov, L. Hassan, N. Ahmad, N. Conci, Natural disasters detection in social media and satellite imagery: a survey. *Multimedia Tools and Applications*. 78(22), 31267-31302 (2019).
- [7] K. RAVINDRA, S. MOR, Rapid monitoring and evaluation of a community-led total sanitation program using smartphones. *Environmental Science and Pollution Research*. 25(32), 31929-31934 (2018).
- [8] A. J. Zellmer, H. Burdick, I. Medel, I. Pondella, T. Ford, Aerial surveys and distribution models enable monitoring of fishing in Marine Protected Areas. *Ocean Coastal Management*. 165, 298-306 (2018).
- [9] Super strong earth scanner-"Hongqi-1-H9" wide satellite began on-orbit debugging. Available online: <https://xw.qq.com/cmsid/20200116A0V8GI00> (accessed on 27 May 2020).
- [10] L. L. Wang, B. Yang, P. Zheng, W. S. Guan, H. Y. Wang, On-orbit relative radiometric calibration method of video satellite. *Infrared and Laser Engineering*. 47(8), 7003-7009 (2018).
- [11] Chang Guang Satellite Technology Co., LTD. Available online: <http://www.charmingglobe.com/> (accessed on 29 May 2020).
- [12] J. H. Lim, J. W. Lee, T. K. Ryu, H. C. Lee, S. G. Lee, Optimal Design of the Reflector Antenna to Improve Performance of C-Band Quad-Pol ScanSAR Systems. *Journal of Electromagnetic Engineering and Science*, 20(2), 155-157 (2020).
- [13] J. P. Jhan, J. Y. Rau, N. Haala, M. Cramer, Investigation of parallax issues for multi-lens multispectral camera band co-registration. *The International Archives of Photogrammetry, Remote Sensing and Spatial Information Sciences*. 42, 157-163 (2017).
- [14] G. Zhang, K. Xu, P. Jia, X. Hao, D. R. Li, Integrating Stereo Images and Laser Altimeter Data of the ZY-02 Satellite for Improved Earth Topographic Modeling. *Remote Sensing*. 11(20), 2453-2470 (2019).
- [15] Q. Y. Meng, H. Y. Wang, Z. Q. Yan, Residual aberration correction method of the three-mirror anastigmat (TMA) system with a real exit pupil using freeform surface. *Optics Laser Technology*. 106, 100-106 (2018).
- [16] L. G. COOK, Wide field of view three-mirror anastigmat (TMA) employing spherical secondary and tertiary mirrors. Recent Trends in Optical Systems Design and Computer Lens Design Workshop. *International Society for Optics and Photonics*. 158-162 (1987).
- [17] V. I. Zavarzin, Y. S. Mitrofanova, System solutions for prospective hyperspectral equipment. *Journal of Optical Technology*. 84(4), 226-230 (2017).
- [18] M. Wang, Y. Zhu, S. Jin, J. Pan, Q. Zhu, Correction of ZY-3 image distortion caused by satellite jitter via virtual steady reimaging using attitude data. *ISPRS Journal of Photogrammetry and Remote Sensing*. 119, 108-123 (2016).
- [19] H. B. Pan, C. Tao, Z. R. Zou, Precise georeferencing using the rigorous sensor model and rational function model for ZiYuan-3 strip scenes with minimum control. *ISPRS Journal of Photogrammetry and Remote Sensing*. 119, 259-266 (2016).
- [20] W. C. Huang, G. Zhang, D. R. Li, Robust approach for recovery of rigorous sensor model using rational function model. *IEEE Transactions on Geoscience and Remote Sensing*. 54(7), 4355-4361 (2016).
- [21] R. L. Kirk, J. M. Barrett, D. E. Wahl, I. Erteza, C. V. Jackowatz, D. A. Yocky, G. W. Paterson, A Semi-Rigorous Sensor Model for Precision Geometric Processing of Mini-RF Bistatic Radar Images of the Moon. *The International Archives of Photogrammetry, Remote Sensing and Spatial Information Sciences*, (41) 425-441 (2016).
- [22] K. Al-Durgham, D. D. Lichti, G. Kuntze, J. Ronsky, Rigorous accuracy assessment for 3D reconstruction using time-series Dual Fluoroscopy (DF) image pairs. *Videometrics, Range Imaging, and Applications XIV. International Society for Optics and Photonics*. 10332, 203-209 (2017).

- [23] S. Liu, X.H. Tong, F. Wang, W. Sun, C. Guo, Z. Ye, P. Chen, Attitude Jitter Detection Based on Remotely Sensed Images and Dense Ground Controls: A Case Study for Chinese ZY-3 Satellite. *IEEE Journal of Selected Topics in Applied Earth Observations and Remote Sensing*.9(12), 5760-5766(2016).
- [24] H.B. Pan, S.Y. Zou, L.Y. Guan, Block Adjustment with Drift Compensation for Rational Function Model. *Photogrammetric Engineering Remote Sensing*.84(12),791-799(2018).
- [25] X. Ling, Y. Zhang, J. Xiong, X. Huang, Z. Chen, An Image Matching Algorithm Integrating Global SRTM and Image Segmentation for Multi-Source Satellite Imagery, *Remote Sensing*, 8(8),747-763(2016).
- [26] S. Hou, Y. Huang, G. Zhang, R. Zhao, P. Jia, Feasibility of Replacing the Range Doppler Equation of Spaceborne Synthetic Aperture Radar Considering Atmospheric Propagation Delay with a Rational Polynomial Coefficient Model. *Sensors*.20(2),553-569(2020).
- [27] K. Di, B. Liu, M. Jia, Z. Liu, Geopositioning precision analysis of multiple image triangulation using LRO NA Lunar images. *The International Archives of Photogrammetry, Remote Sensing and Spatial Information Sciences*.41,369-387(2016).
- [28] H.B. Pan, S.Y. Zou, L.Y. Guan, Block Adjustment with Drift Compensation for Rational Function Model. *Photogrammetric Engineering Remote Sensing*. 84(12),791-799(2018).
- [29] Z.H. ZHONG, S.Xu, Y. Zhang, Y. Han, L. Xu, Rational polynomial coefficients generation for high resolution Ziyuan-3 imagery. 2017 IEEE 14th International Conference on Networking, Sensing and Control (ICNSC). 691-695(2017).
- [30] X.H. Tong, S.J. Liu, H. Xie, H. Wang, P. Chen, F. Bao, Geometric integration of aerial and QuickBird imagery for high accuracy geopositioning and mapping application: A case study in Shanghai. *Marine Geodesy*.33(4),437-449(2010).
- [31] C. B. Liu, D. Li, N. Xue, Surveying Satellite Imagery RPC Block Adjustment without Ground Control Points, *Hydrographic Surveying and Charting*.38(6),17-20(2018).
- [32] C. Li, X. Liu, Y. Zhang, Z. Zhang, A stepwise-then-orthogonal regression (STOR) with quality control for optimizing the RFM of high-resolution satellite imagery. *Photogrammetric Engineering Remote Sensing*. 83(9), 611-620(2017).
- [33] S.J. Tang, B. WU, Q. Zhu. Combined adjustment of multi-resolution satellite imagery for improved geo-positioning accuracy. *ISPRS journal of photogrammetry and remote sensing*.114,125-136(2016).
- [34] Y. H. Jiang, J. Y. Wang, L. Zhang, G. Zhang, X. Li, J. Q. Wu, Geometric Processing and Accuracy Verification of Zhuhai-1 Hyperspectral Satellites. *Remote Sensing*. 11(9),996-1013(2019).
- [35] B. Yang, M. Wang, Y.D. Pi, Block-adjustment without GCPs for Large-scale Regions only Based on the Virtual Control Points. *Acta Geodaetica et Cartographica Sinica*.46(7),139-151(2017).
- [36] B.W. Liu, X.J. Duan, L. Yan, A Novel Bayesian Method for Calculating Circular Error Probability with Systematic-Biased Prior Information. *Mathematical Problems in Engineering*.2018,1-10(2018).
- [37] D.E. Chaitanya, L. Ganesh, G.S. Rao, Performance analysis of hyperbolic multilateration using circular error probability. *Procedia Computer Science*. 85,676-682(2016).
- [38] C.H. Grohmann, Evaluation of TanDEM-X DEMs on selected Brazilian sites: Comparison with SRTM, ASTER GDEM and ALOS AW3D30. *Remote Sensing of Environment*.212,121-133(2018).
- [39] B. Wessel, M. Huber, C. Wohlfart, U. Marschalk, D. Kosmann, A. Roth. Accuracy assessment of the global TanDEM-X Digital Elevation Model with GPS data. *ISPRS Journal of Photogrammetry and Remote Sensing*. 139,171-182(2018).
- [40] D. B. Gesch, D. F. Maune, Digital elevation model technologies and applications: the DEM users manual. The national elevation dataset, 2nd edn. American Society for Photogrammetry and Remote Sensing, Bethesda. 99-118(2007).

#### Figures

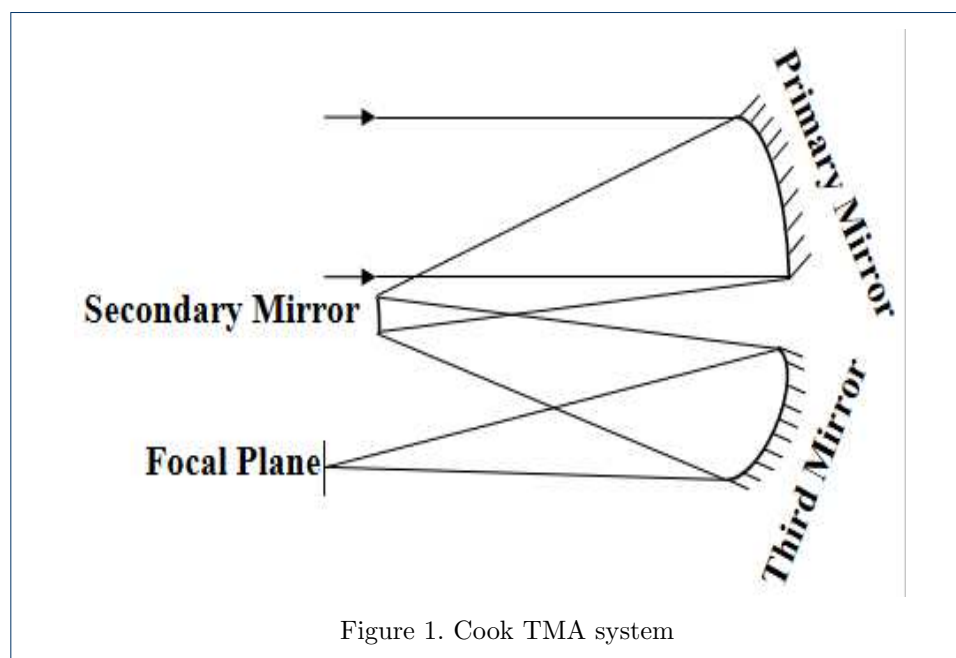


Figure 1. Cook TMA system

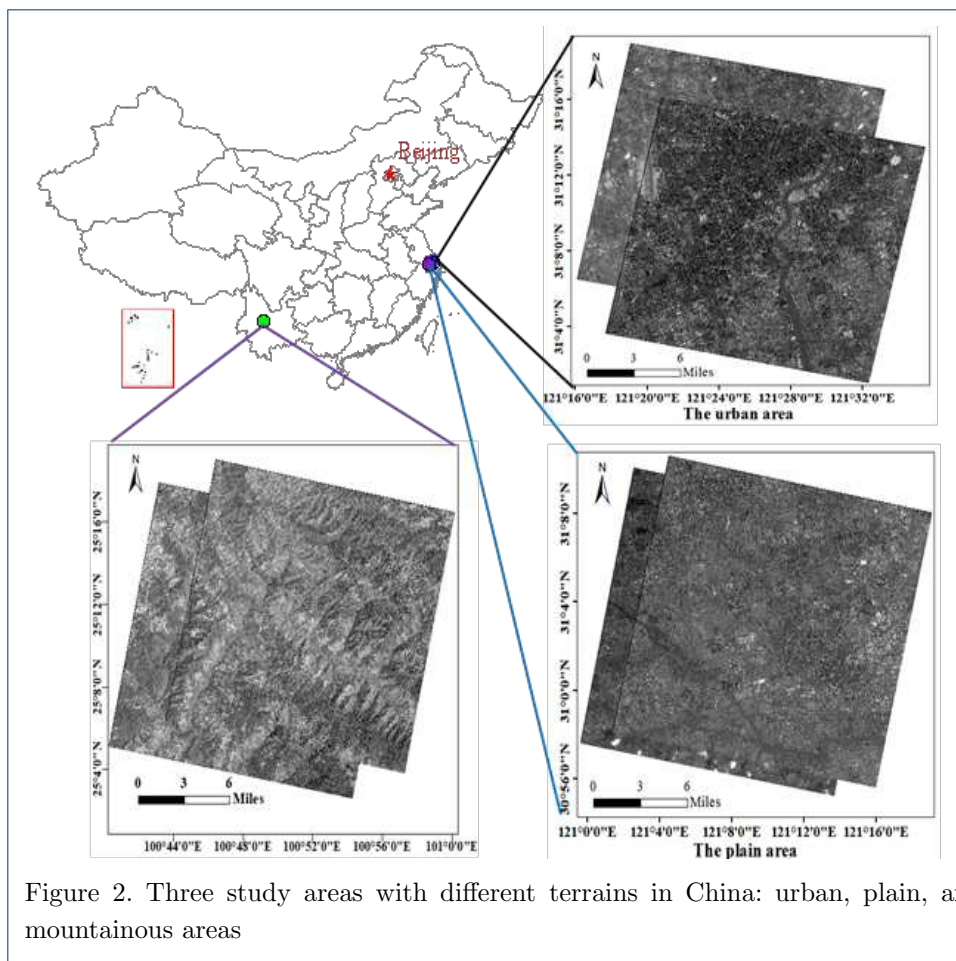


Figure 2. Three study areas with different terrains in China: urban, plain, and mountainous areas

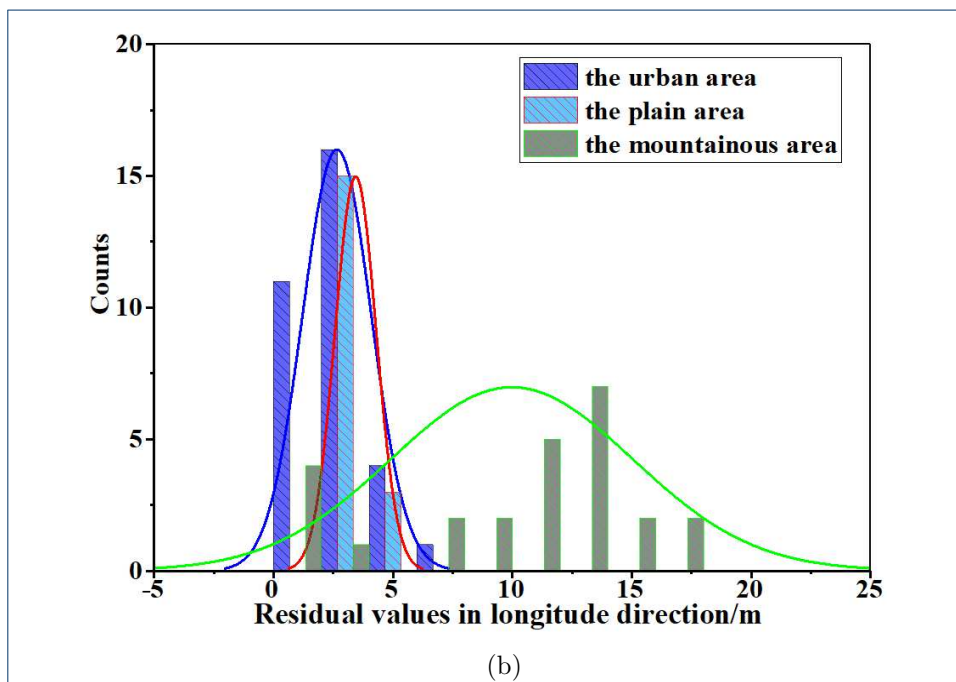
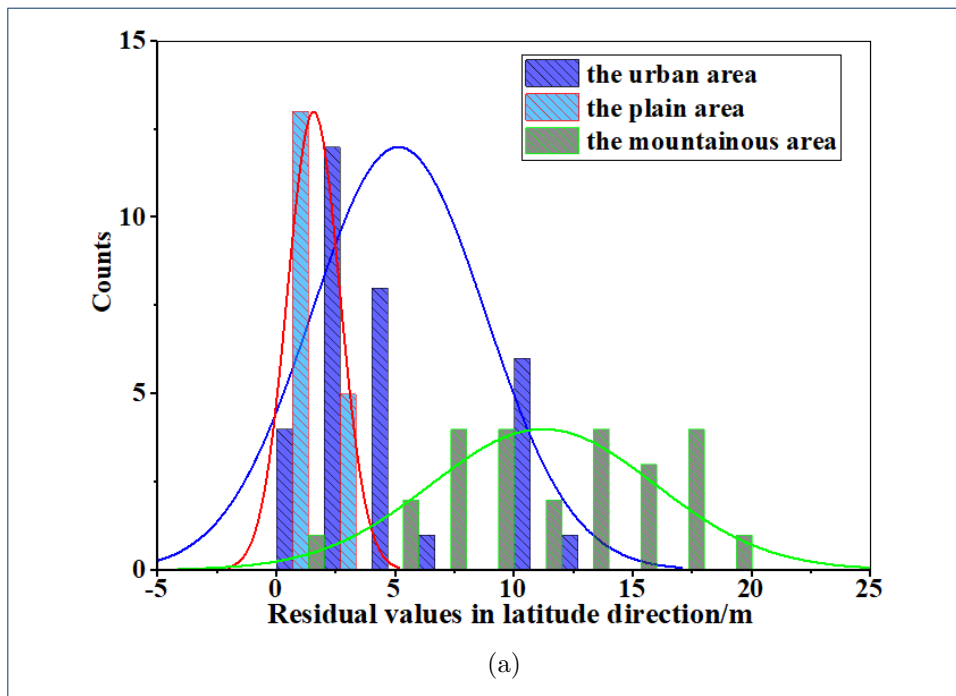
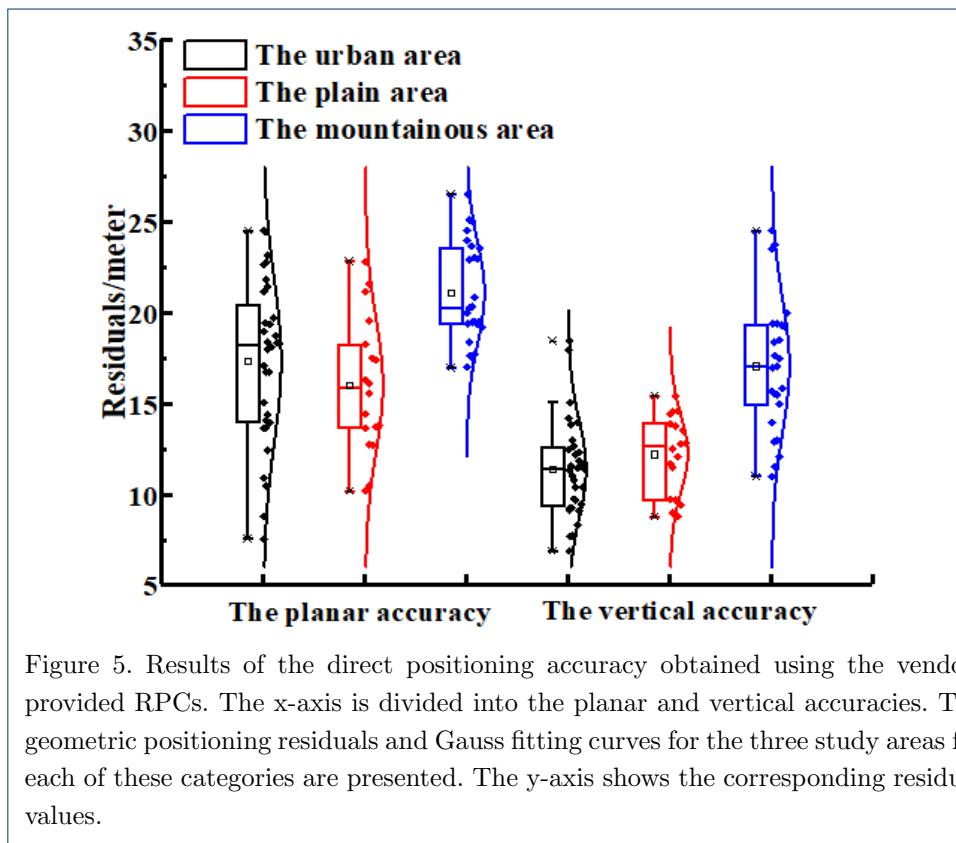
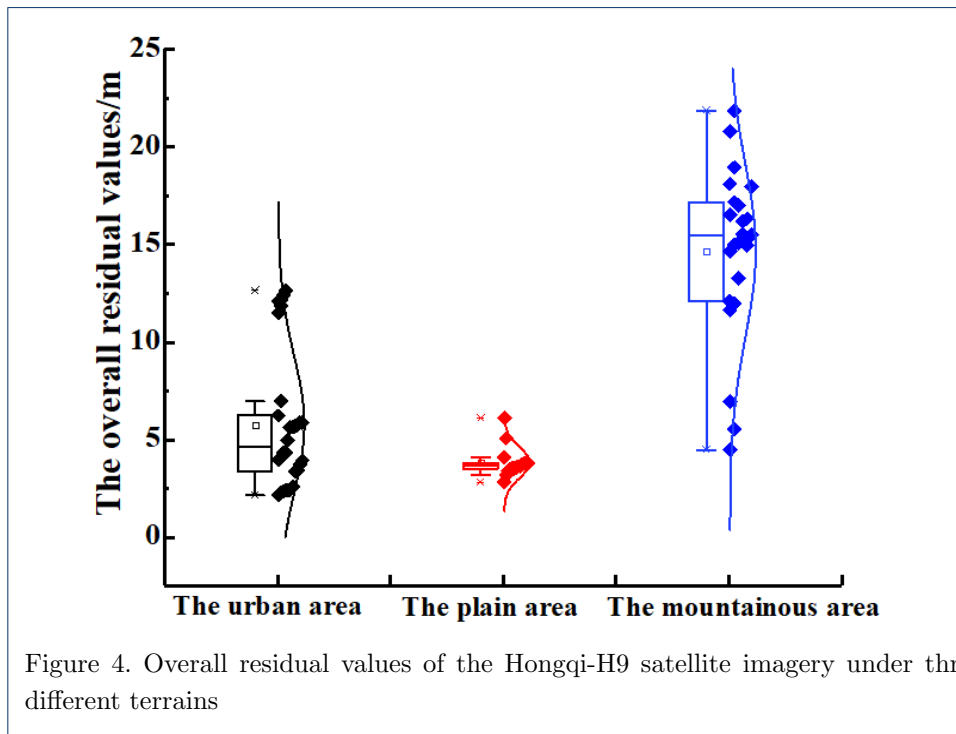
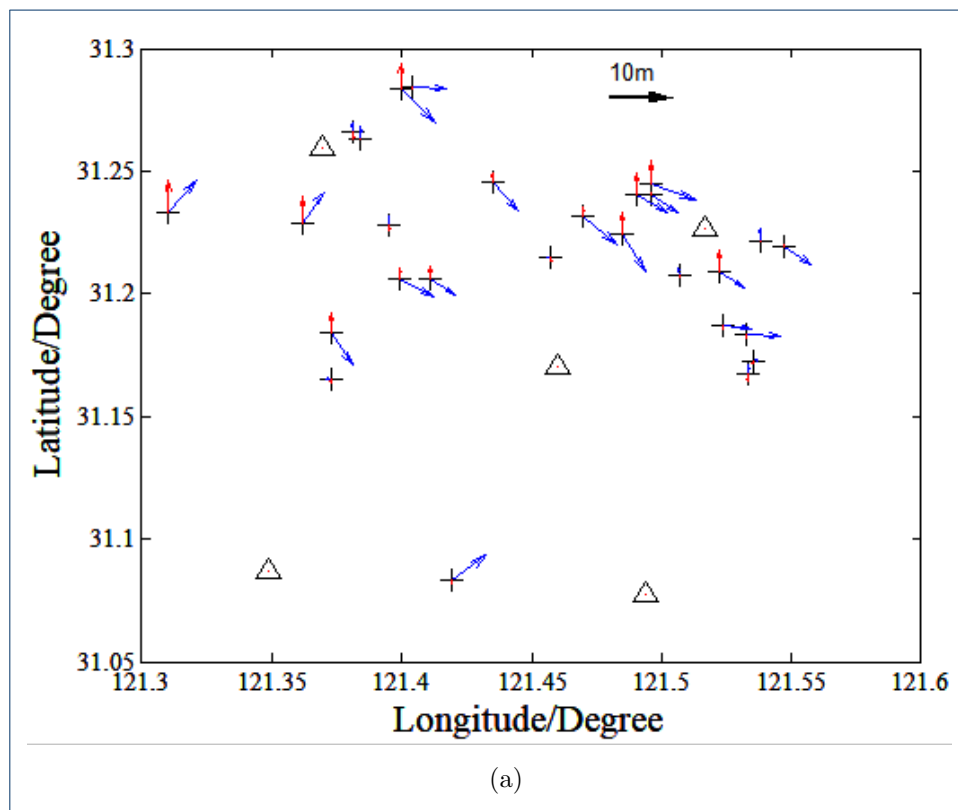
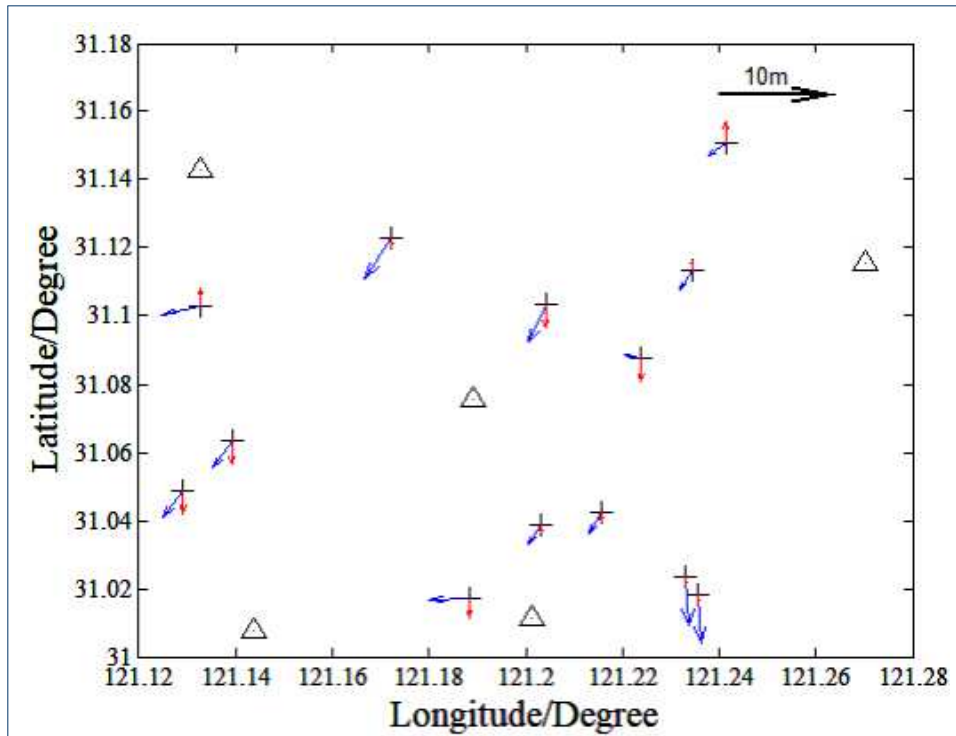


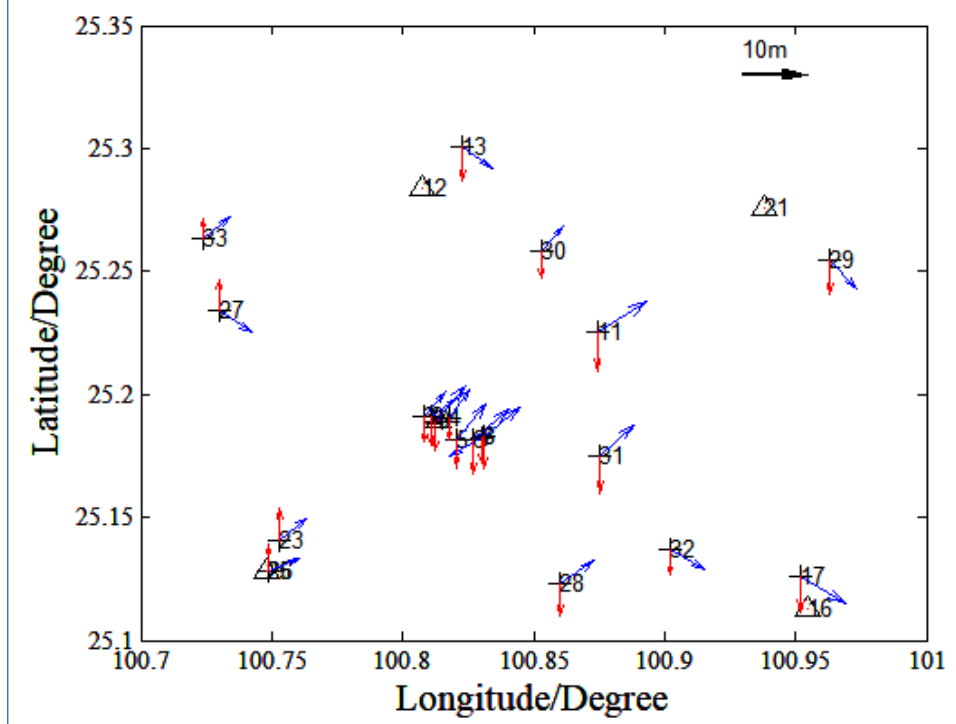
Figure 3. Residuals of the Hongqi-H9 imagery under three different terrains in the (a) latitude and (b) longitude directions. The x and y axes correspond to the residual values of the three different study areas and the corresponding residual counts, respectively. The residual fitting results for the Hongqi-H9 satellite imagery under three different terrains, obtained using the normal distribution functions are also presented.







(b)



(c)

Figure 6. Geometric positioning error bar graphs when using five GCPs. The black crosses represent the point positions in the WGS84 coordinate system, and the blue and red arrows indicate the plane and elevation errors, respectively. (a), (b) and (c) show the results for the urban, plain, and mountainous areas, respectively.

# Figures

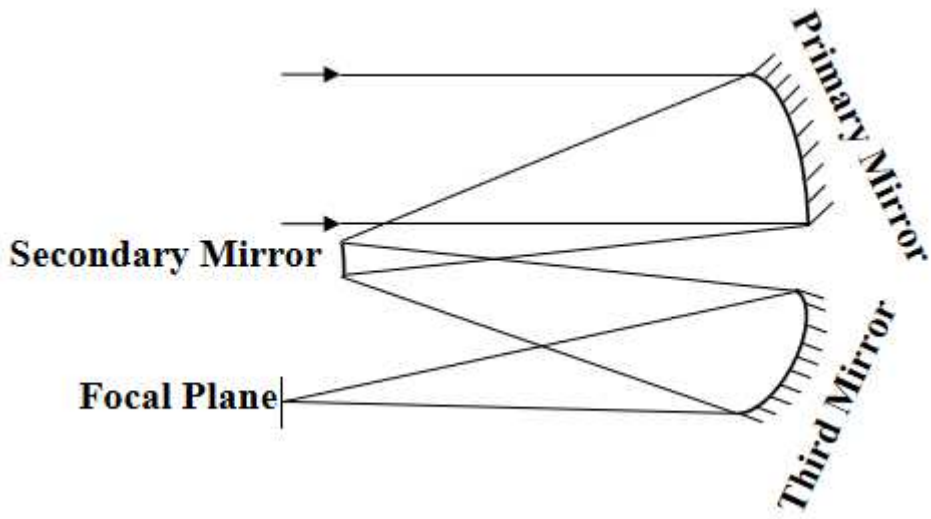
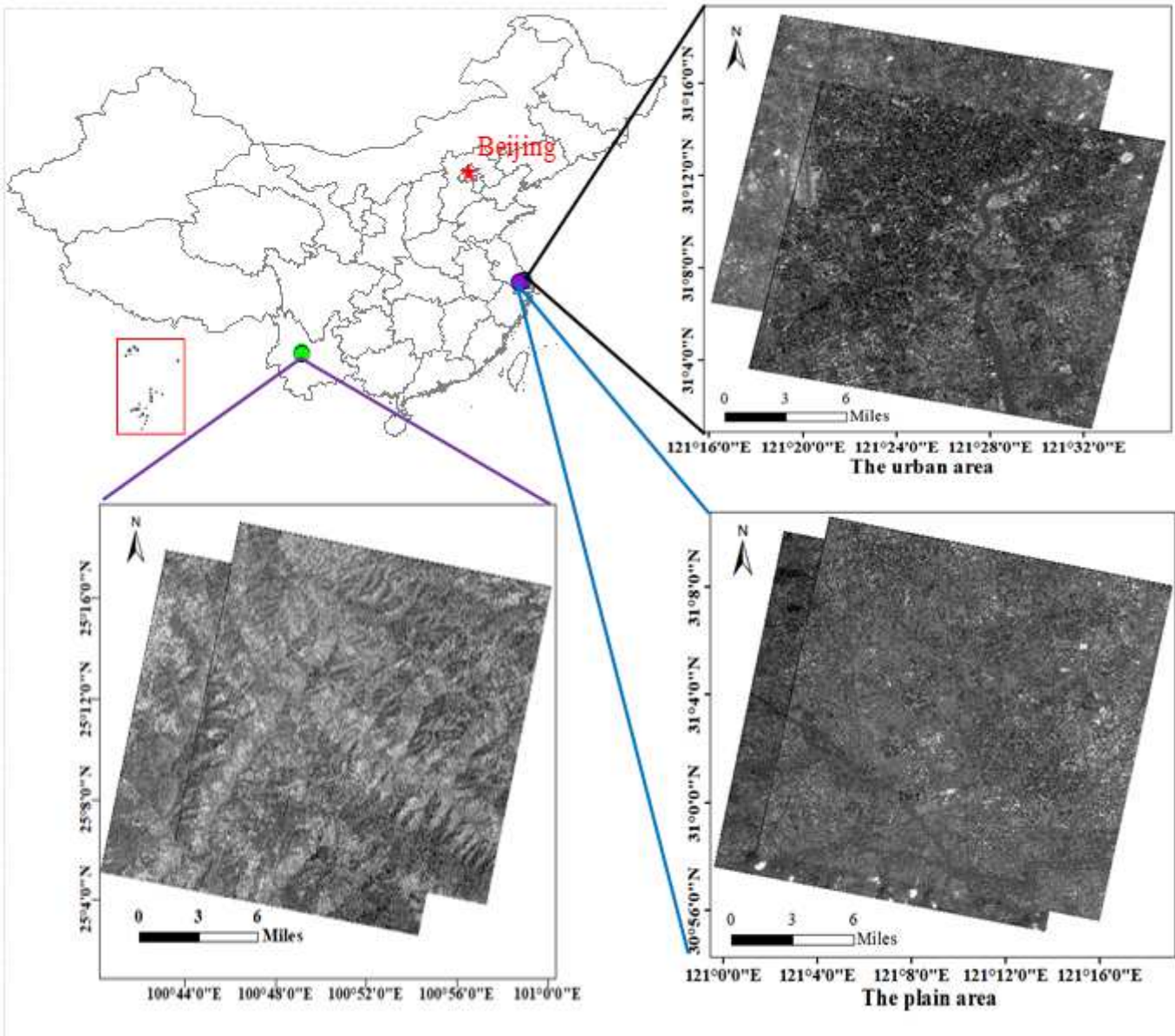


Figure 1

Cook TMA system



**Figure 2**

Three study areas with different terrains in China: urban, plain, and mountainous areas Note: The designations employed and the presentation of the material on this map do not imply the expression of any opinion whatsoever on the part of Research Square concerning the legal status of any country, territory, city or area or of its authorities, or concerning the delimitation of its frontiers or boundaries. This map has been provided by the authors.

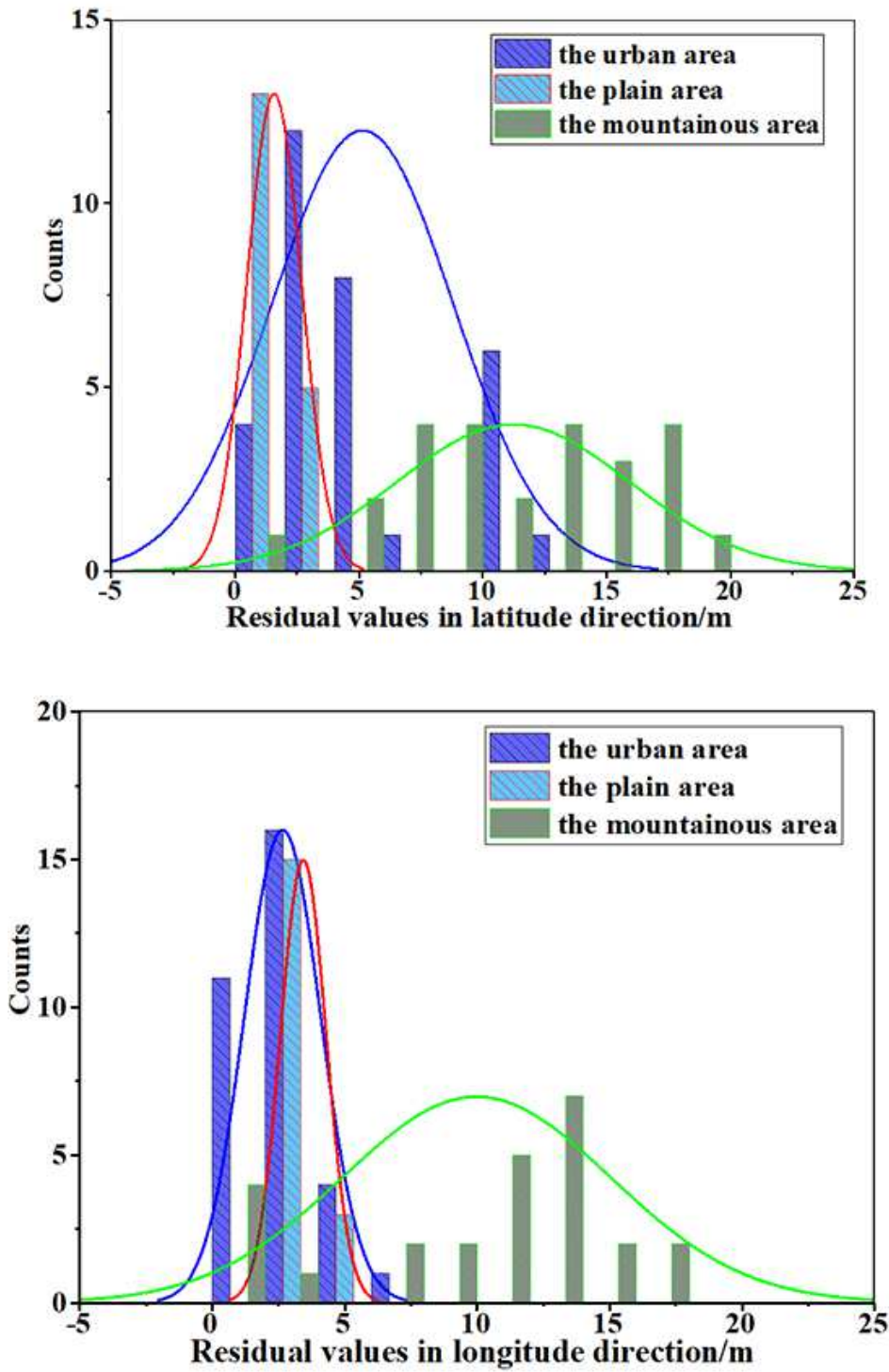


**Figure 3**

Residuals of the Hongqi-H9 imagery under three different terrains in the (a) latitude and (b) longitude directions. The x and y axes correspond to the residual values of the three different study areas and the corresponding residual counts, respectively. The residual fitting results for the Hongqi-H9 satellite imagery under three different terrains, obtained using the normal distribution functions are also presented.

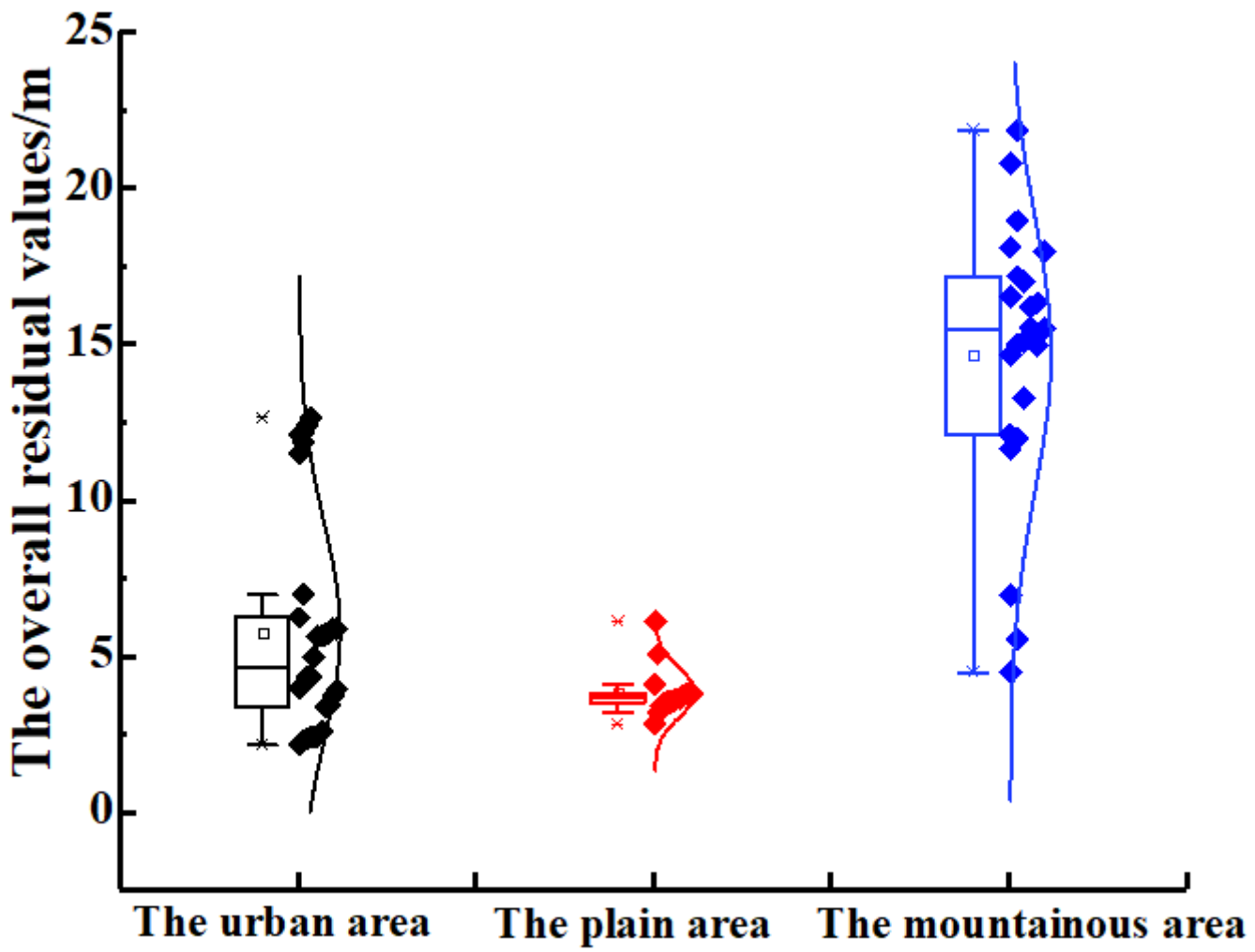


Figure 4

Overall residual values of the Hongqi-H9 satellite imagery under three different terrains

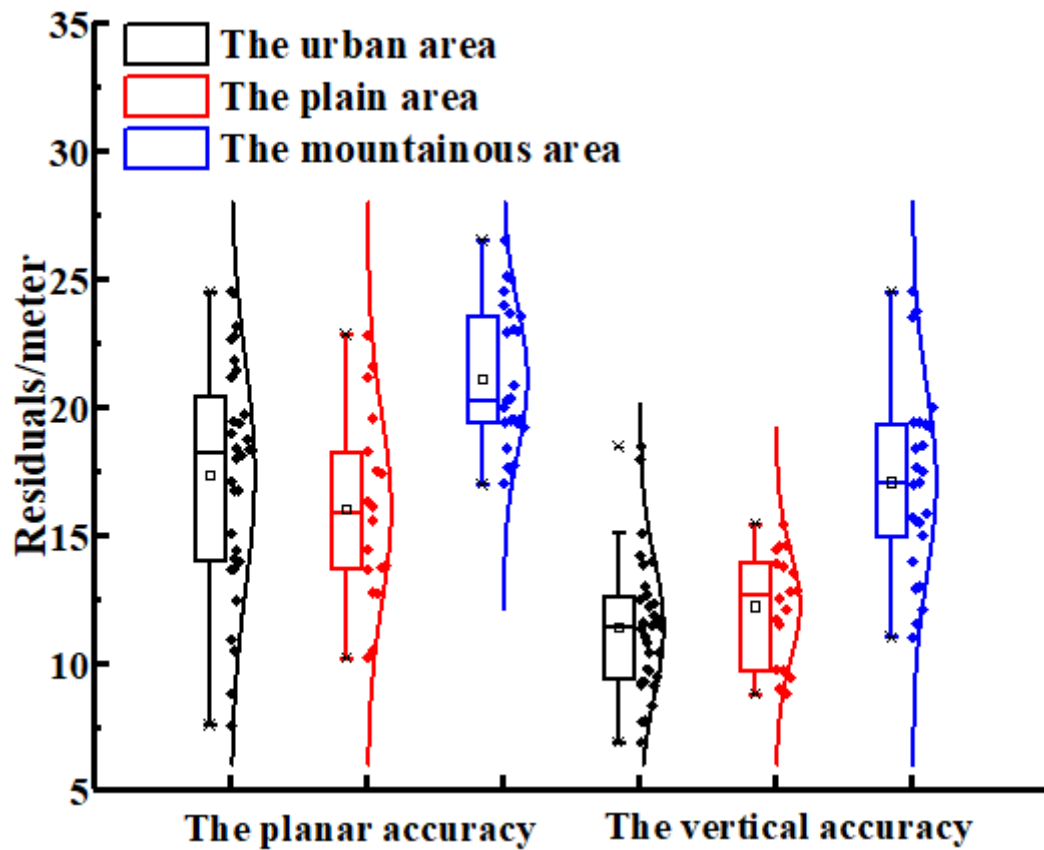
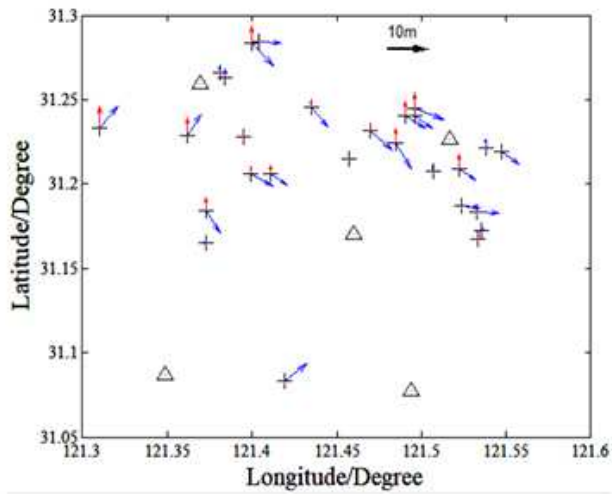
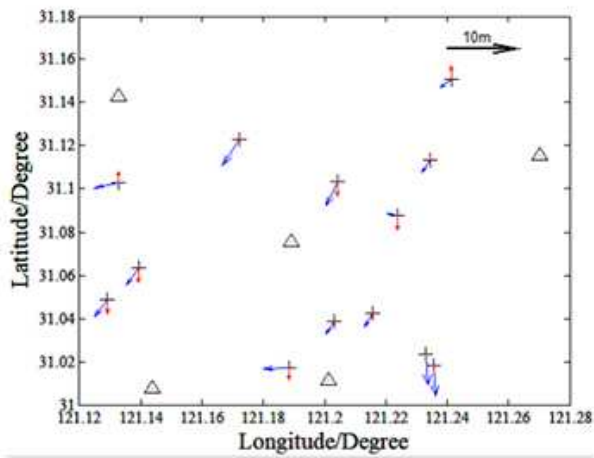


Figure 5

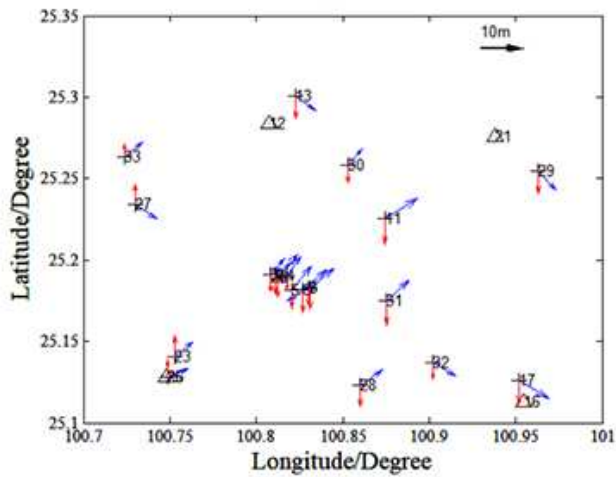
Results of the direct positioning accuracy obtained using the vendor-provided RPCs. The x-axis is divided into the planar and vertical accuracies. The geometric positioning residuals and Gauss fitting curves for the three study areas for each of these categories are presented. The y-axis shows the corresponding residual values.



(a)



(b)



(c)

**Figure 6**

Geometric positioning error bar graphs when using ve GCPs. The black crosses represent the point positions in the WGS84 coordinate system, and the blue and red arrows indicate the plane and elevation errors, respectively. (a), (b) and (c) show the results for the urban, plain, and mountainous areas, respectively.